Simple Postsynthesis Thermal Treatment toward High Luminescence Performance of Rare Earth Vanadate Nanoparticles

Rafael Vieira Perrella, Rabei Mohammedi, Robin Kuhner, Christophe Cardone, Eric Larquet, Antigoni Alexandrou, Paulo Cesar de Sousa Filho, Thierry Gacoin

Simple post-synthesis thermal treatment towards high luminescence performance of rare earth vanadate nanoparticles

Rafael V. Perrella,[†,§] Rabei Mohammedi,[†] Robin Kuhner,[‡] Christophe Cardone,[‡] Eric Larquet,[†] Antigoni Alexandrou,[‡] Paulo Cesar de Sousa Filho,[§,] Thierry Gacoin[†,*]*

[†]Laboratoire de Physique de la Matière Condensée, Ecole Polytechnique, Institut Polytechnique de Paris, CNRS, Route de Saclay, 91128 Palaiseau, France

[§]Department of Inorganic Chemistry, Institute of Chemistry, University of Campinas (Unicamp), R. Monteiro Lobato, 270, 13083-970, Campinas, São Paulo, Brazil

[‡]Laboratoire d'Optique et Biosciences, Ecole Polytechnique, Institut Polytechnique de Paris, CNRS, INSERM, Route de Saclay, 91128 Palaiseau, France

ABSTRACT: Optical applications of colloidal oxide nanoparticles are often limited by low luminescence efficiencies caused by poor crystallinity and surface quenching. Bulk oxides prepared via conventional high-temperature annealing offer intense luminescence but commonly fail to yield stable colloidal dispersions. Coupling the best of these two situations to afford highly crystalline, dispersible nanoparticles with luminescence performance exceeding bulk solids is still challenging, thus requiring new safe, scalable, and reproducible methodologies. Herein we report a silicate-coating strategy followed by aggregate elimination to recover stable colloids of 40-150 nm single crystalline rare earth vanadates after unprotected annealing (800-1000 °C). Eu^{3+}-doped nanoparticles showed enhanced photostability and ~50% emission quantum yields in water (λ_{exc}=280 nm), while Dy^{3+}-, Tm^{3+}-, and Yb^{3+}/Er^{3+}-doped vanadates provided remarkably intense multicolour emissions via downshift or upconversion luminescence. We correlated spectroscopic properties of pristine and annealed solids to microstructural characteristics to explain the superior emission features, opening new perspectives for sensing applications.

High-temperature annealing of solid-state precursors is a generally convenient method to produce bulk oxides with high crystalline quality.[1–3] Such methods are still widespread for large-scale production of light-emitting materials with high quantum yields suitable for applications. Nevertheless, the emergence of sophisticated applications demanding isolated and colloidally stable nanoparticles imposes significant barriers for further exploration of these conventional techniques.[4–6] Liquid-phase synthesis starting from homogeneous or micro-heterogeneous precursors can be applied to produce 10-100 nm inorganic oxides with a controlled size distribution.[7–9] However, the poor crystallinity, high surface area, and high defect density of the obtained nanoparticles are often detrimental in terms of luminescence.[10,11] Combining colloidal stability and high crystalline quality requires a delicate balance during annealing post-treatments to preserve the nanostructural character without irreversible aggregation while eliminating surface and lattice defects.

This challenge also applies for rare earth (RE) vanadates ($REVO_4$), which are a versatile class of dual ultraviolet (UV)- and near-infrared (NIR)-excitable luminescent oxide materials.[12,13] On the one hand, applications of $REVO_4$ in chemical sensing[14] and biomimetic catalysis[15] usually explore the effects of polycrystallinity, porosity, and of defect density of nanoparticles. On the other hand, applications in nanothermometry,[11,16] light-emitting coatings,[17] and bioimaging[18] demand luminescence efficiencies and photostability ideally approaching those of bulk materials, thus requiring nearly single crystalline nanoparticles. For example, while pristine Eu^{3+}-doped YVO_4 nanoparticles show a <10% overall quantum yield in water, a bulk solid with the same composition may show yields as high as 70%.[19] Therefore, there is room for significant enhancement of the luminescence performance of colloidal nanoparticles via strategies to improve particle crystallinity while keeping nanosized dimensions. In many cases, however, post-treatments in suspension (i.e.,

hydro- or solvothermal) are not completely efficient for crystalline improvement,[10] and temperatures higher than 700 °C are often necessary.[20] To overcome particle sintering induced by the high-temperature treatment, we developed protected annealing approaches[10,11,20,21] where inert silica hosts act as diffusional barriers to prevent particle aggregation at 900-1000 °C. In these protocols, well crystallised and readily dispersible nanoparticles can be recovered after the dissolution of the silica host by hydrofluoric acid, which imposes significant drawbacks concerning safety and scale-up. In addition, the chemical stability of pristine particles towards the acidic silica sol and the reactivity of final particles to form rare earth tri- or tetrafluorides by HF attack are also important issues.

In the present work, we are revisiting a straightforward thermal treatment of pristine nanoparticle powders obtained through conventional colloidal coprecipitation. The idea is to determine the possibility of achieving a thermal treatment ensuring the internal reconstruction of the particles while limiting interparticle sintering. The result would be the production of colloidal suspensions of individual nanocrystals through a facile process exhibiting ultimate emission performances close to the bulk material. This protocol can be further simplified assuming that, despite aggregation effects, initial $REVO_4$ particles can keep the original dimensions after annealing, and further redispersion and size selection can be performed to remove large aggregates by controlling the surface characteristics of the solids.

We therefore report the production of highly crystalline and colloidally stable $REVO_4$ (40-150 nm) particles after unprotected annealing of pristine (~30 nm) nanoparticles (Figure 1). We discuss how the luminescence performance can be enhanced in terms of quantum yields, resistance towards decreasing luminescence intensity under UV irradiation, and multicolour emissions via

downshift and upconversion, thus correlating the spectroscopic behaviour to the microstructure of as-prepared and annealed particles.

Preparation of pristine $REVO_4$ nanoparticles comprised direct coprecipitation in water at 25 °C starting from RE nitrates and sodium metavanadate as described in previous papers[22,23] (experimental procedures and general characterisation are detailed in the Supporting Information, SI). The as-prepared particles consist of arrangements of monocrystalline grains into anisotropic polycrystalline assemblies (Figure 1a) with axial dimensions of 14 ± 3 nm and 32 ± 6 nm and mean hydrodynamic diameters of 37 ± 9 nm (Figure 1g and Figure S1). The primary grains have the characteristic tetragonal $I4_1/amd$ structure as shown by powder XRD (Figure 1b), with average crystalline coherence lengths of 6 ± 1 nm (Figure 1g) and high crystal strain (0.0042 ± 0.0008, Table S1). The ratio between coherence lengths in the [001] and [100] directions is ~1.5 (Table S1), confirming the prolate shape anisotropy of the crystallites forming the $REVO_4$ nanoparticles obtained through direct coprecipitation.

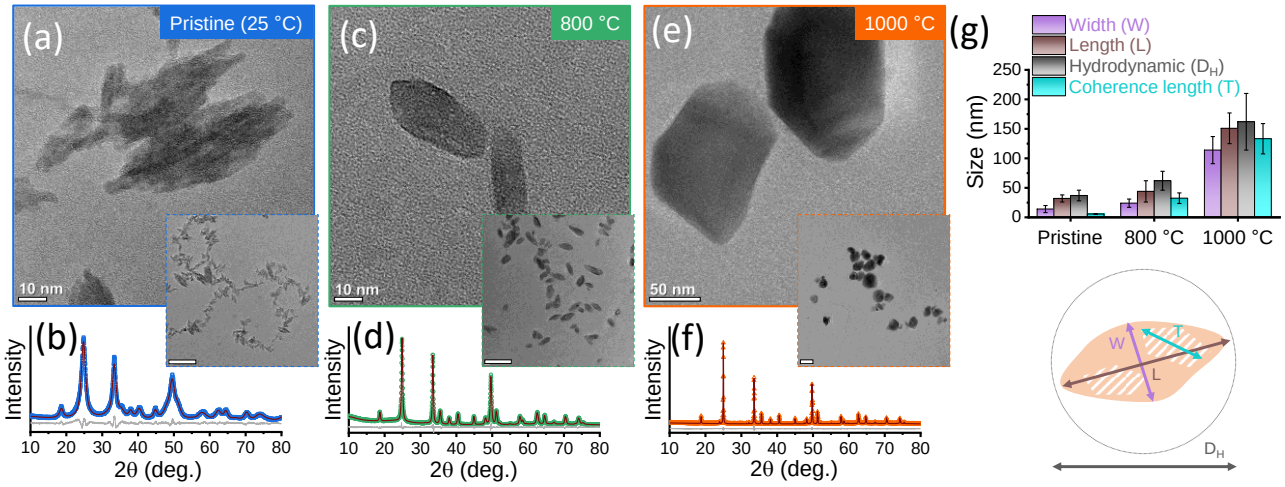

Figure 1. (a,c,e) TEM images, (b,d,f) powder X-ray diffractograms, and (g) size distributions of (a,b) pristine and (c-f) annealed $Y_{0.95}Eu_{0.05}VO_4$ nanoparticles [(c,d) 800 °C, (e,f) 1000 °C] obtained after the size selection process. Insets in (a,c,e) correspond to low magnification TEM images for

size analysis (scale bars correspond to 100 nm (a,c) and 200 nm (e)). Points, red and grey lines in (b,d,f) correspond respectively to experimental data, fitted diffraction profiles, and residuals after Rietveld refinements using MAUD software (Table S1). Widths/lengths (W/L), hydrodynamic diameters (D_H), and coherence lengths (T) in (g) were determined from TEM images, dynamic light scattering, and XRD refinements, respectively. Size distributions are shown in Figure S1.

Unprotected annealing of pristine $REVO_4$ particles at 800 or 1000 °C produced dense micrometric agglomerates where isolated particles were still observed (Figure S2), suggesting that highly crystalline nanoparticles could be recovered from aggregates via adequate processing. We proposed an acid treatment of these aggregates to induce partial disaggregation of the solids to enable the recovery of electrostatically stabilised isolated nanoparticles via differential centrifugation. Indeed, readily dispersible high-crystallinity nanoparticles (Figure 1c-f) with low size polydispersity were recovered after annealing at 800 and 1000 °C by a 48 h acid treatment followed by surface stabilisation by metasilicates (optimised protocols for particle recovery are described in detail in the SI). Differential centrifugation of final suspensions enabled to select the mean particle sizes by screening centrifugation speed (Figures S3, S4, and S5). The recovery yield determined by X-ray fluorescence spectrometry was ~2% (mol/mol, based on an initial concentration of 50 mmol L^{-1} of vanadate ions) for both treatments at 800 and 1000 °C, and the acid treatment step was shown to be crucial to provide the disaggregation of the annealed nanoparticles (Figure S6). The recovery yields could be improved to ~20% by previous milling of aggregates generated after annealing (Figure S7). Nevertheless, even though this improvement can be interesting for particles for other applications (*e.g.* catalysis), the milling step resulted in a

drastic decrease in luminescence efficiency due to heavy plastic deformation of the solids, possibly inducing large amounts of crystalline defects (Figure S7d).

Finally, we also applied the optimised protocols in an attempt to recover $REVO_4$ nanoparticles from an annealed solid produced by the conventional solid-state reaction between Y_2O_3 and V_2O_5 (Supporting Information). The results confirmed that metasilicate stabilisation combined with milling only enabled the recovery of submicrometric particles in this case (~720 nm, Figure S8), which confirms that the pre-existence of pristine solids with a small size is essential to allow the recovery of small size, highly crystalline and colloidally stable vanadates particles via the proposed methodology. The results discussed hereafter refer to pristine particles (Figure 1a,b) annealed at 800 or 1000 °C and further purified by double centrifugation at 121*g* for 5 min and 400*g* for 5 min without milling steps to afford low-polydispersity colloidal suspensions (SI).

The annealed particles obtained after the recovery steps showed highly charged surfaces ($\zeta \sim -45$ mV at pH ~ 9) due to surface coating with metasilicates (Figure S9). The solids obtained after annealing at 800 °C (Figure 1c, Figure S1d) kept the elongated shape of the initial particles (axial dimensions of 24 ± 7 nm and 44 ± 18 nm) with a smoother surface and reduced porosity. Structural alterations also comprised an increase in average coherence length to 32 ± 8 nm, higher shape anisotropy (~2.1), and reduced strain (0.0011 ± 0.0002, Table S1). Considering the dimensions of the initial pristine $REVO_4$ particles (~30 nm), such an increase in coherence lengths is likely due to the intraparticle sintering of their internal primary grain structure rather than interparticle growth, leading to crystalline improvement with a minor alteration of particle size. Further heating at temperatures higher than the Tamman temperature (*i.e.* $T_{Tamman} = 0.5T_{melting}$, $T_{Tamman} \sim 905$ °C for YVO_4)[24] provides enough energy for increased atomic diffusion, leading to interparticle sintering. This explains why particles produced after annealing at 1000 °C underwent a larger

growth (114 ± 23 nm and 151 ± 26 nm, Figure 1e, Figure S1f) and assumed a more isotropic morphology, which is also confirmed by the lower shape anisotropy (1.2, Table S1). Comparing the dimensions of the particles recovered after treatment at 1000 °C and the corresponding crystalline coherence lengths (133 ± 25 nm Figure 1g), we demonstrate that the protocol yielded nearly monocrystalline nanoparticles with faceted planes and reduced microstrain ((1.9 ± 0.9) x 10^{-4}, Table S1). The annealing also impacts lattice parameters, where pristine particles showing expanded unit cells due to surface defects[9,24–26] undergo progressive unit cell constriction after heating at 800 and 1000 °C (Table S1).

The use of Eu^{3+} as a luminescent probe provided further insights on the crystalline quality of the nanoparticles (Figure 2). The excitation bands (Supporting Information) due to VO_4^{3-} absorptions ($^1T_{2,1} \leftarrow {}^1A_1$, 250-350 nm) followed by $VO_4^{3-} \rightarrow Eu^{3+}$ energy transfer were affected by the crystallinity and microstructure (Figure S10, Table S2). The annealed solids showed red-shifted barycentres of the excitation bands and higher intensity of the low-energy component ($^1T_1 \leftarrow {}^1A_1$) in comparison to pristine particles. This agrees with the energy stabilisation of VO_4^{3-} states due to increased covalence caused by the reduction of lattice parameters.[27,28] UV-excitation (λ_{exc} = 280 nm) yielded the characteristic emissions of Eu^{3+} in YVO_4 comprising the typical $^5D_0 \rightarrow {}^7F_J$ (J = 0–4) transitions (Figure 2a) with similar profiles for pristine and annealed particles. Concerning absolute emission intensities (Figure S11), the impact of the crystalline improvement is evident comparing the overall quantum yields of the YVO_4:Eu^{3+} nanoparticles (SI). The initial emission yield of 9% raised to 38% after annealing at 800 °C and to 49% at 1000 °C, considering 50 µmol L^{-1} aqueous suspensions (concentration in vanadate ions). These values compare favourably with other YVO_4:Eu^{3+} particles[19,29] and represent some of the highest overall quantum yields reported for colloidal lanthanide-based nano- and submicroparticles. The difference between quantum

yields of the highly crystalline annealed particles (49%) and of bulk solids (70%)[30] is due to the intrinsically lower emission probability of nanoparticles due to the lower effective refractive index of the aqueous solvent with respect to that of the $YVO_4:Eu^{3+}$ solid.[19] Hence, the annealing process provides highly bright nanophosphors showing the best emission properties that can be expected for $YVO_4:Eu^{3+}$ particles dispersed in water.

Detailed analysis of Stark components provided further correlations to microstructural properties. Because Eu^{3+} ions occupy D_{2d} sites in the $I4_1/amd$ structure, the $^7F_2$ state splits into A_1, B_1, B_2, and E Stark levels, which gives rise to two forced electric dipole components of the $^5D_0 \rightarrow {}^7F_2$ transition (Figure 2a-c, Table S3), namely $^5D_0 \rightarrow {}^7F_2(B_2)$ (~614 nm) and $^5D_0 \rightarrow {}^7F_2(E)$ (~618 nm). Previous reports[9,31] suggest that the larger inhomogeneous broadening of these components is related to the lower long-range crystalline quality of the solids. In turn, the relative intensities between these two peaks correlate to the angular distortion of the Eu^{3+} coordination polyhedra in YVO_4,[9] where distortions of the D_{2d} symmetry provide a higher contribution of the A_1 component resulting in an intensification of the high energy peak (*i.e.* $^5D_0 \rightarrow {}^7F_2(B_2)$).[32] Our results confirm these observations with annealed solids showing approximately the same bandwidth (~1.5 nm), narrower than that of pristine particles (>2.3 nm, Figure 2b). In addition, the as-prepared particles with increased defect densities showed more pronounced microsymmetry distortion around Eu^{3+} ions, resulting in higher relative intensities of the B_2 components in comparison to the annealed solids (Figure 2b). This behaviour was also found analysing the Judd-Ofelt intensity parameters (Ω_2 and Ω_4),[33] which showed a progressive decrease with the annealing temperature (Figure 2d, Table S4). The Ω_2 parameter is related to angular distortions around the Eu^{3+} microsymmetry, and the Ω_4 is more sensitive to linear distortions of europium-ligand bonds.[33] Hence, heat treatment largely removed lattice distortions in the synthesised pristine $REVO_4$ particles. In addition, the effects of lattice

contraction upon annealing involve a higher orbital overlap in V-O bonds, which in turn results in slightly more ionic RE-O bonds as indicated by Ω_4 values. The distortions of non-annealed solids also cause the presence of the $^5D_0 \rightarrow {}^7F_0$ transition in the emission spectrum of pristine particles (Figure 2a). This transition is forbidden in D_{2d} symmetry (Table S3), and its occurrence is an evidence that part of the Eu^{3+} ions occupy distorted sites. Indeed, the $^5D_0 \rightarrow {}^7F_0$ signal vanishes after annealing (Figure 2a). As pointed out by Riwotzki *et al.*,[34] these distorted sites are mostly related to surface Eu^{3+} ions, which is also in agreement with the higher surface area of pristine particles in comparison to annealed solids. When the pristine particles are transferred from H_2O to D_2O suspensions (Supporting Information), the luminescence quenching promoted by surface OH groups becomes less effective, leading to an intensification of Eu^{3+} emissions.[19] We observed that the intensity enhancement was higher for the $^5D_0 \rightarrow {}^7F_0$ emission (Figure S12), which attests to the surface nature of the distorted sites originating this transition.

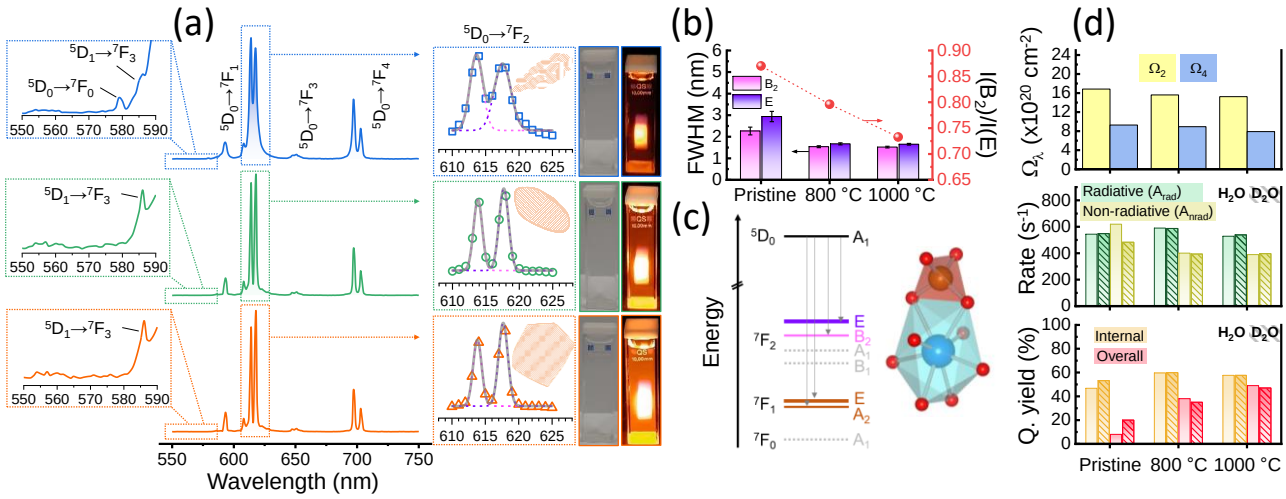

Figure 2. (a) Emission spectra (λ_{exc} = 280 nm) of pristine (blue, top) and annealed (800 °C, green, middle; 1000 °C, orange, bottom) $Y_{0.95}Eu_{0.05}VO_4$ nanoparticles as 50 µmol L^{-1} aqueous suspensions (concentration in vanadate ions). Excitation spectra are shown in Figure S10. Insets at the left represent amplifications of the region between 550 and 590 nm, indicating the $^5D_1 \rightarrow {}^7F_3$

and $^5D_0 \rightarrow {}^7F_0$ transitions. Insets at the right show amplifications of the $^5D_0 \rightarrow {}^7F_2$ transition (610-625 nm) and photographs of particle colloids under white light and UV excitation. Experimental data of $^5D_0 \rightarrow {}^7F_2$ emissions (points) were deconvoluted into two Gaussian peaks corresponding to B_2 (rose lines) and E (purple lines) Stark components. (b) Values of full width at half maximum (FWHM, left) and the intensity ratio between the two Stark components ($I(B_2)/I(E)$, right) calculated from deconvolution of the $^5D_0 \rightarrow {}^7F_2$ signals. (c) Schematic energy level diagram of Eu^{3+} representing the Stark components of $^5D_0$ and ^7F_J (J = 0-2) levels for a D_{2d} symmetry and coordination polyhedral for V and RE in tetragonal YVO_4. (d) Judd-Ofelt intensity parameters (Ω_2 and Ω_4, top), radiative and non-radiative decay rates (A_{RAD}, A_{NRAD}, middle), and overall and internal quantum yields (bottom) of pristine and annealed $Y_{0.95}Eu_{0.05}VO_4$ nanoparticles. Decay rates and quantum yields were measured both as suspensions in H_2O (no pattern) and D_2O (diagonal pattern). $^5D_0$ luminescence lifetimes and data analysis details are found in the Supporting Information.

We also evaluated the luminescence of the $YVO_4:Eu^{3+}$ particles in terms of radiative and non-radiative decay probabilities of the Eu^{3+} $^5D_0$ state based on emission spectra and luminescence lifetimes (Supporting Information) in H_2O and D_2O. To ensure reliable comparisons, we analysed particles having nearly the same surface state, which was achieved by a silicate coating on the pristine particles. This functionalisation provided surface modification without affecting the morphology, microstructure, and emission properties of pristine particles (Figure S13). While as-prepared particles resulted in bi-exponential decay curves due to surface and defect-distorted sites, the annealed particles fitted well for single exponential decays yielding lifetimes of 1.01 ms (800 °C) and 1.09 ms (1000 °C) (Table S4, Figure S14). The mean $^5D_0$ lifetime of pristine particles in

H_2O (0.86 ms) increased to 0.97 ms upon dispersion in D_2O, while annealed particles showed approximately constant lifetimes in H_2O and D_2O due to their higher stability towards surface quenching (Table S4). Radiative decay rates (A_{RAD}) were roughly constant within <8% for all particle suspensions both in H_2O (554 ± 24 s^{-1}) and D_2O (558 ± 19 s^{-1}, Figure 2d). This confirms that the microstructure has a minor effect on the radiative probabilities of the Eu^{3+} emissions, and changes in the local refractive indices are negligible due to the low volume fraction of the particles in aqueous suspensions.[19] By contrast, solvent exchange and annealing strongly affected non-radiative decay rates (A_{NRAD}, Figure 2d), with an expected decrease in A_{NRAD} values when pristine particles are transferred into D_2O. The annealed particles showed constant A_{NRAD} values regardless of whether H_2O or D_2O were used as solvents, showing limited surface/solvent interactions in these cases without the necessity of using complex core@-shell structures prepared by multiple growths. Consequently, the reduction of non-radiative decay rates due to enhancement in crystallinity through annealing led to higher internal (η) and overall quantum yields (q_{EXP}, Figure 2d). Even though a small variation of η values is observed comparing particles annealed at 800 and 1000 °C, the significant increase in q_{EXP} confirms the positive results of further crystalline improvement towards nearly monocrystalline nanoparticles. Ultimately, the high overall quantum yields also reflect the high efficiency of the energy migration between VO_4^{3-} groups and the $VO_4^{3-} \rightarrow Eu^{3+}$ energy transfer process.

We explored the versatility of the proposed methodology to produce green and blue emitting nanophosphors in addition to Eu^{3+}-doped vanadates (Figure 3). Dy^{3+}, Tm^{3+}, and Er^{3+} dopants have a more complex energy level structure which makes these activators even more sensitive than Eu^{3+} towards luminescence quenching by crystalline defects, and surface water/OH groups. Consequently, pristine $YVO_4:Dy^{3+}$ and $YVO_4:Tm^{3+}$ particles show rather inefficient downshift

luminescence (Figure 3a,b), while no upconversion emissions could be observed for as-prepared $YVO_4:Yb^{3+},Er^{3+}$ particles under ~80 W cm^{-2} excitation (λ_{exc} = 980 nm). However, colloids of nanocrystalline $YVO_4:Ln^{3+}$ (Ln^{3+} = Dy^{3+}, Tm^{3+}) produced after annealing at 800 or 1000 °C showed significant enhancement of luminescence intensities in comparison to pristine solids. The excitation spectra (Figure S15) of Dy^{3+}- and Tm^{3+}-doped particles are nearly identical to the spectra for $YVO_4:Eu^{3+}$ particles (Figure S10), confirming that YVO_4 enables efficient sensitization regardless of the dopant ions as long as the crystalline improvement minimises the different quenching channels.

Accordingly, enhancement of the crystallinity of $YVO_4:Yb^{3+},Er^{3+}$ particles allowed upconversion emissions under excitation at λ_{exc} = 980 nm in water suspension (Figure 3c,d). The typical Er^{3+} emissions in the green (525 nm and 553 nm, $^2H_{11/2}\rightarrow{}^4I_{15/2}$ and $^4S_{3/2}\rightarrow{}^4I_{15/2}$) and red (659 nm, $^4F_{9/2}\rightarrow{}^4I_{15/2}$) regions were observed by the naked eye at pump powers as low as 11 W cm^{-2}, which is hardly achieved for oxide-based nanoparticles suspensions.[11,35] The upconversion intensities increased biexponentially with pump power (Figure 3d), with slopes close to the theoretical value of 2 photons expected for the population of the Er^{3+} $^2H_{11/2}$ and $^4S_{3/2}$ emitting states (1.8 and 1.7, respectively). A negative deviation from the expected slope of 2 (0.8) was verified for the population of the $^4F_{9/2}$ level, which is due to the high Yb/Er ratio.[36]

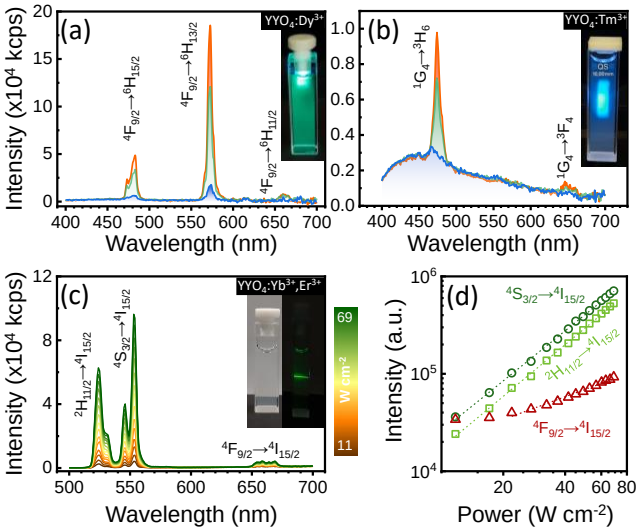

Figure 3. Downshift emission spectra of (a) $Y_{0.95}Dy_{0.05}VO_4$ and (b) $Y_{0.95}Tm_{0.05}VO_4$ solids under λ_{exc} = 280 nm. Blue, green, and orange lines refer to pristine particles and solids annealed at 800 °C, and 1000 °C, respectively. Spectra in (a) and (b) were acquired for nanoparticles as 50 µmol L^{-1} aqueous suspensions (concentration in vanadate ions) in an integrating sphere. Insets in (a) and (b) show photographs of suspensions of particles annealed at 1000 °C under UV irradiation (λ_{exc} = 280 nm). Excitation spectra are shown in Figure S15. (c) Upconversion (λ_{exc} = 980 nm) spectra of $Y_{0.78}Yb_{0.20}Er_{0.02}VO_4$ particles annealed at 1000 °C as aqueous colloids (250 µmol L^{-1}, concentration in vanadate ions) under different pump powers (11 to 69 W cm^{-2}). The inset in (c) shows photographs of $YVO_4:Yb^{3+},Er^{3+}$ particle suspensions under white light and under NIR excitation at 81 W cm^{-2}. (d) Power dependence of integrated intensities of $^2H_{11/2}\rightarrow{}^4I_{15/2}$ (525 nm, squares), $^4S_{3/2}\rightarrow{}^4I_{15/2}$ (553 nm, circles), and $^4F_{9/2}\rightarrow{}^4I_{15/2}$ (659 nm, triangles) calculated from spectra in (c).

In addition to the enhancement of luminescence intensities and quantum yields, the crystalline improvement also enabled the decrease of the degree of luminescence loss as a function of

irradiation time associated with UV-excitation in the prepared $REVO_4$ nanoparticles (Figure 4). Despite the common comparison with organic fluorophores to affirm that lanthanide emissions do not present luminescence decrease as a function of irradiation time, the complex redox and defect chemistry of some oxide nanoparticles together with interactions with the solvent may also cause progressive quenching of Ln^{3+} emissions under UV irradiation.[37] For instance, Eu^{3+}-doped $REVO_4$ aqueous colloids show a decrease in luminescence under UV excitation due to the reduction of the host matrix (V^{5+}/V^{4+}) or the reduction of the activator ion (Eu^{3+}/Eu^{2+}).[38,39] A reversible photoreduction of Eu^{3+} upon direct Eu^{3+} excitation or a reversible chemical reduction of $GdVO_4$:Eu^{3+} particles was observed and exploited by us to implement reactive oxygen species-sensitive nanosensors.[14,40,41] Moreover, the luminescence of Tb^{3+} in YVO_4 also decreases under UV irradiation due to the partial oxidation of vacancies in air.[26]

We therefore compared the time evolution of Eu^{3+} luminescence in pristine and annealed YVO_4 nanoparticles under constant UV LED irradiation (λ_{exc} = 280 nm, I = 4.4 mW cm^{-2}), monitoring both particles in PBS buffer (Figure 4a) and solids deposited on nitrocellulose membranes (Figure 4b). Whilst as-prepared colloidal particles retained only 37 ± 4% of the initial luminescence intensity after 5 min of light exposition, solids annealed at 800 and 1000 °C kept 70 ± 4% and 87 ± 5% of the initial signal, respectively. This UV-induced quenching is visually observed in the nitrocellulose membranes (Figure 4b), resulting in similar time evolution of emissions (Figure S16). We attribute this remarkable enhancement of photostability to a balance between surface area, crystallinity, and particle size. Firstly, crystalline improvement provides a lower density of V^{4+} centres that facilitate the Eu^{3+}/Eu^{2+} photoreduction and the consequent quenching of Eu^{3+} emissions. Second, the heat treatment leads to a reduced porosity, which diminishes the interactions of Eu^{3+} ions with the solvent. Also, the larger size of annealed solids results in lower

fractions of illuminated ions per volume of particle, considering that the penetration depth of the UV photons is nearly constant for pristine and annealed particles (*i.e.* constant absorption coefficients).

The enhanced photostability of annealed particles in the colloidal state is also confirmed for more chemically aggressive aqueous conditions, namely at pH = 1 (HNO_3), pH = 13 (NaOH), and 0.5 mol L^{-1} hydrogen peroxide (Figure 4c-e). The luminescence of pristine particles at pH = 1 is almost totally quenched after 5 min of UV irradiation (Figure 4c) mainly due to partial dissolution. This effect is nearly eliminated for the colloidal nanocrystals obtained after annealing at 1000 °C (Figure 4e). Interestingly, the alkaline conditions and the presence of hydrogen peroxide altered the emission evolution of pristine particles (Figure 4c), probably due to the oxidative removal of oxygen vacancies and reduced vanadium species by OH^- and OH• species or to the reoxidation of photoreduced europium ions due to the interaction with H_2O_2.[14,40,41] Altogether, these results confirm the necessity of single crystalline particles for photochemically stable colloids and the efficiency of the proposed methodology to improve the luminescence efficiency of vanadate nanoparticles.

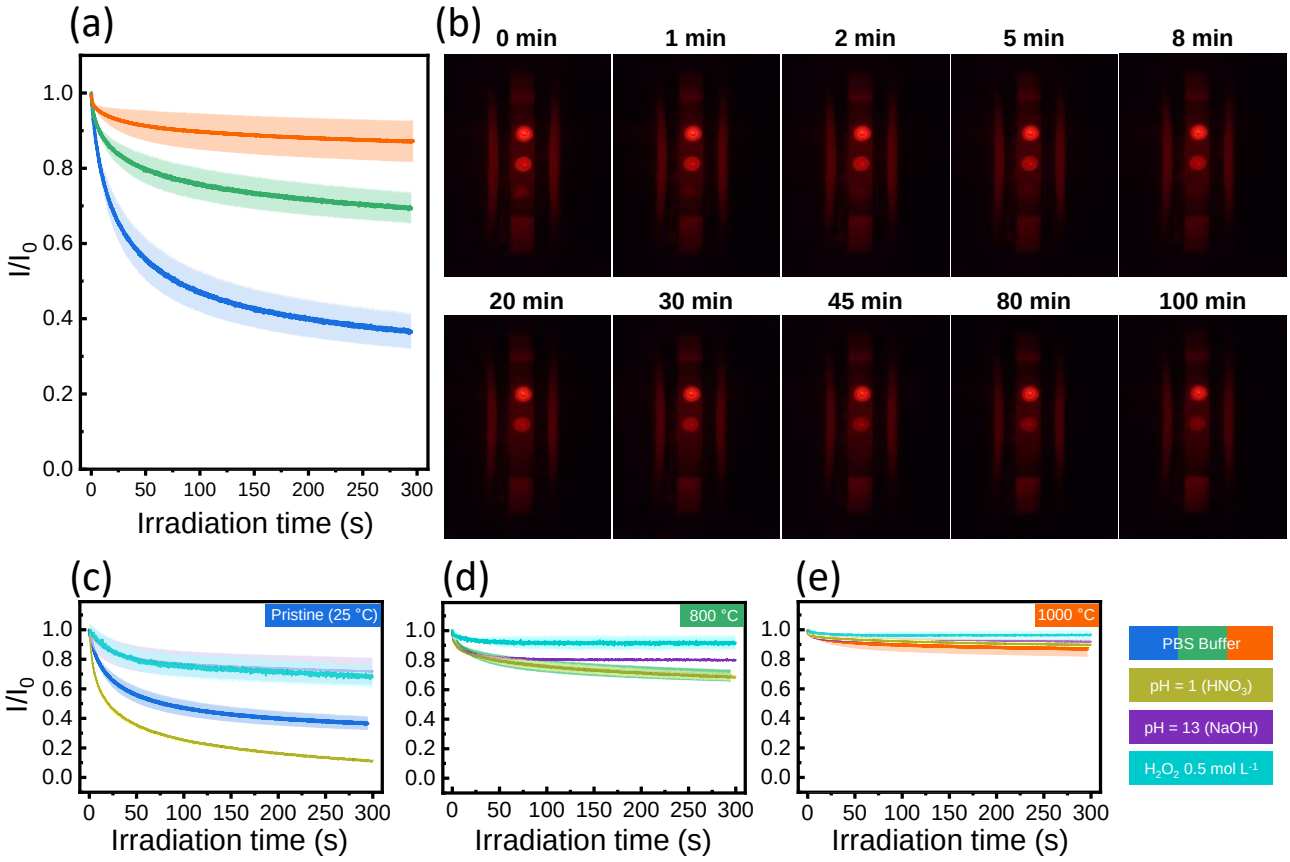

Figure 4. Photostability of $Y_{0.95}Eu_{0.05}VO_4$ particles in aqueous suspensions under UV irradiation (λ_{exc} = 280 nm, I = 4.4 mW cm^{-2}). (a) Evolution of the luminescence intensity of particles in PBS buffer against the irradiation time for pristine solids (blue) and particles annealed at 800 °C (green) and 1000 °C (orange). Experimental data correspond to solid lines, and standard deviations are shown as shaded areas. Additional details are found in the SI. (b) Photographs of nitrocellulose membranes containing drops of particle suspensions under irradiation at different times (top to bottom: particles annealed at 1000 °C, particles annealed at 800 °C, and pristine particles). (c-e) Effect of the dispersing medium on the photostability of (c) pristine, (d) 800 °C, and (e) 1000 °C annealed $Y_{0.95}Eu_{0.05}VO_4$ particles. The decrease of luminescence intensities with the irradiation time was measured for particles in PBS (blue, green, or orange lines, same data as in (a)) in

comparison to particles in HNO_3 (pH = 1, dark yellow), NaOH (pH = 13, purple), or 0.5 mol L^{-1} hydrogen peroxide (cyan) solutions.

Our results ultimately demonstrate a simple method for preparing highly crystalline $REVO_4$ particles with 40-150 nm size by the unprotected annealing of pristine ~30 nm nanoparticles followed by acid treatment and silicate coating. The reduced defect density coupled with limited surface quenching enhances both photostability and luminescence efficiency under UV excitation, resulting in one of the highest quantum yields reported so far for oxide-based colloidal particles (*i.e.* 38 and 49% after annealing at 800 and 1000 °C, respectively). Green (Dy^{3+}-doped), blue (Tm^{3+}-doped), and upconverting (Yb^{3+}/Er^{3+}-doped) nanoparticles with intense UV- or NIR-excited luminescence are successfully obtained by the same route. Hence, we demonstrate that multiple types of emissions can be achieved in highly crystalline $REVO_4$ nanoparticles, thus expanding the applicability of these solids towards applications requiring high light output, such as ultrasensitive *in vitro* diagnosis or light-emitting coatings.

ASSOCIATED CONTENT

Supporting Information

The Supporting Information is available free of charge at https://pubs.acs.org.

Detailed experimental procedures, size and ζ potential distributions, additional TEM images, X-ray diffractograms and results of data refinement, FTIR spectra, luminescence spectra, and calculated spectroscopic parameters (PDF)

AUTHOR INFORMATION

Corresponding Author

Paulo Cesar de Sousa Filho – Department of Inorganic Chemistry, Institute of Chemistry, University of Campinas (Unicamp), R. Monteiro Lobato, 270, 13083-970, Campinas, São Paulo, Brazil. Email: pcsfilho@unicamp.br

Thierry Gacoin – Laboratoire de Physique de la Matière Condensée, Ecole Polytechnique, Institut Polytechnique de Paris, CNRS, Route de Saclay, 91128 Palaiseau, France. Email: thierry.gacoin@polytechnique.edu

Author Contributions

The manuscript was written through contributions of all authors. All authors have given approval to the final version of the manuscript.

Notes

The authors declare no competing financial interests.

ACKNOWLEDGMENT

The authors acknowledge the agencies CAPES, CNPq, FAEPEX-PrP-Unicamp, and FAPESP (Proc. 2017/19909-0 and 2019/23398-6 R.V.P.) for financial support and scholarships, and FAPESP/ANR (2022/03442-3 P.C.d.S.F.) for international collaboration funding. This work has also been partially funded by a public grant from ANR (Agence National de la Recherche), project 3D-NanoREV number ANR-22-CE08-0027-01, and AID (Agence Innovation Defense) project DAVID reference 2020-65-0055.

REFERENCES

(1) *Phosphor Handbook*, 2nd ed.; Yen, W. M., Shionoya, S., Yamamoto, H., Eds.; CRC Press: Boca Raton, 2007.

(2) Ronda, C. C. R. *Luminescence: From Theory to Applications*; Wiley-VCH: Weinheim, 2008.

(3) Blasse, G.; Grabmaier, B. C. *Luminescent Materials*; Springer-Verlag: Berlin, 1994.

(4) Abid, N.; Khan, A. M.; Shujait, S.; Chaudhary, K.; Ikram, M.; Imran, M.; Haider, J.; Khan, M.; Khan, Q.; Maqbool, M. Synthesis of Nanomaterials Using Various Top-down and Bottom-up Approaches, Influencing Factors, Advantages, and Disadvantages: A Review. *Adv. Colloid Interface Sci.* **2022**, *300*, 102597.

(5) Mousseau, F.; Féraudet Tarisse, C.; Simon, S.; Gacoin, T.; Alexandrou, A.; Bouzigues, C. I. Luminescent Lanthanide Nanoparticle-Based Imaging Enables Ultra-Sensitive, Quantitative and Multiplexed: In Vitro Lateral Flow Immunoassays. *Nanoscale* **2021**, *13*, 14814–14824.

(6) Zhang, Z.; Jayakumar, M. K. G.; Zheng, X.; Shikha, S.; Zhang, Y.; Bansal, A.; Poon, D. J. J.; Chu, P. L.; Yeo, E. L. L.; Chua, M. L. K.; Chee, S. K.; Zhang, Y. Upconversion Superballs for Programmable Photoactivation of Therapeutics. *Nat. Commun.* **2019**, *10*, 1–12.

(7) Gaspar, R. D. L.; Mazali, I. O.; Sigoli, F. A. Particle Size Tailoring and Luminescence of Europium(III)-Doped Gadolinium Oxide Obtained by the Modified Homogeneous Precipitation Method: Dielectric Constant and Counter Anion Effects. *Colloids Surf. A Physicochem. Eng. Asp.* **2010**, *367*, 155–160.

(8) Jia, Y.; Sun, T.-Y.; Wang, J.-H.; Huang, H.; Li, P.; Yu, X.-F.; Chu, P. K. Synthesis of Hollow Rare-Earth Compound Nanoparticles by a Universal Sacrificial Template Method. *CrystEngComm* **2014**, *16*, 6141–6148.

(9) Guida, G.; Huband, S.; Walker, M.; Walton, R. I.; de Sousa Filho, P. C. Tuning Morphology, Surface, and Nanocrystallinity of Rare Earth Vanadates by One-Pot Colloidal Conversion of Hydroxycarbonates. *Nanoscale* **2021**, *13*, 4931–4945.

(10) Maurin, I.; Dantelle, G.; Boilot, J. P.; Gacoin, T. A Protected Annealing Process for the Production of High Quality Colloidal Oxide Nanoparticles with Optimized Physical Properties. *J. Mater. Chem. C* **2013**, *1*, 13–22.

(11) Perrella, R. V.; de Sousa Filho, P. C. High-Sensitivity Dual UV/NIR-Excited Luminescence Thermometry by Rare Earth Vanadate Nanoparticles. *Dalton Trans.* **2020**, *49*, 911–922.

(12) Chen, C.; Li, C.; Li, T.; Liu, J.; Huang, H.; Bai, T.; Wang, Z.; Shi, Z.; Feng, S. Water-Soluble, Monodisperse, Lanthanide-Doped Y(Gd)VO_4 Nanocrystals as Promising Multimodal Bioprobe. *Eur. J. Inorg. Chem.* **2015**, *2015*, 3108–3115.

(13) Yang, L.; Peng, S.; Zhao, M.; Yu, L. New Synthetic Strategies for Luminescent YVO_4:Ln^{3+} (Ln = Pr, Sm, Eu, Tb, Dy, Ho, Er) with Mesoporous Cell-like Nanostructure. *Opt. Mater. Express* **2018**, *8*, 3805–3819.

(14) Casanova, D.; Bouzigues, C.; Nguyên, T.-L.; Ramodiharilafy, R. O.; Bouzhir-Sima, L.; Gacoin, T.; Boilot, J.-P.; Tharaux, P.-L.; Alexandrou, A. Single Europium-Doped Nanoparticles

Measure Temporal Pattern of Reactive Oxygen Species Production inside Cells. *Nat. Nanotechnol.* **2009**, *4*, 581–585.

(15) Singh, N.; Mugesh, G. $CeVO_4$ Nanozymes Catalyze the Reduction of Dioxygen to Water without Releasing Partially Reduced Oxygen Species. *Angew. Chem. Int. Ed.* **2019**, *58*, 7797–7801.

(16) Marciniak, L.; Bednarkiewicz, A.; Trejgis, K.; Maciejewska, K.; Elzbieciak, K.; Ledwa, K. Enhancing the Sensitivity of a Nd^{3+},Yb^{3+}:YVO_4 Nanocrystalline Luminescent Thermometer by Host Sensitization. *Phys. Chem. Chem. Phys.* **2019**, *21*, 10532–10539.

(17) Dantelle, G.; Fleury, B.; Boilot, J. P.; Gacoin, T. How to Prepare the Brightest Luminescent Coatings? *ACS Appl. Mater. Interfaces* **2013**, *5*, 11315–11320.

(18) Jeyaraman, J.; Shukla, A.; Sivakumar, S. Targeted Stealth Polymer Capsules Encapsulating Ln^{3+}-Doped $LaVO_4$ Nanoparticles for Bioimaging Applications. *ACS Biomater. Sci. Eng.* **2016**, *2*, 1330–1340.

(19) Mialon, G.; Türkcan, S.; Alexandrou, A.; Gacoin, T.; Boilot, J.-P. New Insights into Size Effects in Luminescent Oxide Nanocrystals. *J. Phys. Chem. C* **2009**, *113*, 18699–18706.

(20) Mialon, G.; Gohin, M.; Gacoin, T.; Boilot, J.-P. High Temperature Strategy for Oxide Nanoparticle Synthesis. *ACS Nano* **2008**, *2*, 2505–2512.

(21) de Sousa Filho, P. C.; Gacoin, T.; Boilot, J. P.; Walton, R. I.; Serra, O. A. Synthesis and Luminescent Properties of $REVO_4$-$REPO_4$ (RE = Y, Eu, Gd, Er, Tm, or Yb) Heteronanostructures:

A Promising Class of Phosphors for Excitation from NIR to VUV. *J. Phys. Chem. C* **2015**, *119*, 24062–24074.

(22) Freitas, A. P.; Ramamoorthy, R. K.; Durelle, M.; Larquet, E.; Maurin, I.; Testard, F.; Chevallard, C.; Gacoin, T.; Carriere, D. Crystallization within Intermediate Amorphous Phases Determines the Polycrystallinity of Nanoparticles from Coprecipitation. *Nano Lett.* **2022**, *22*, 29–35.

(23) Neouze, M.-A.; Freitas, A. P.; Ramamoorthy, R.-K.; Mohammedi, R.; Larquet, E.; Tusseau-Nenez, S.; Carrière, D.; Gacoin, T. Toward a Chemical Control of Colloidal YVO_4 Nanoparticles Microstructure. *Langmuir* **2020**, *36*, 9124–9131.

(24) Levin, E. M. The System Y_2O_3-V_2O_5. *J. Am. Ceram. Soc.* **1967**, *50*, 381–382.

(25) Tong, W.; Li, L.; Hu, W.; Yan, T.; Li, G. Systematic Control of Monoclinic $CdWO_4$ Nanophase for Optimum Photocatalytic Activity. *J. Phys. Chem. C* **2010**, *114*, 1512–1519.

(26) Perrella, R. V.; Walker, M.; Chamberlain, T. W.; Walton, R. I.; de Sousa Filho, P. C. The Influence of Defects on the Luminescence of Trivalent Terbium in Nanocrystalline Yttrium Orthovanadate. *Nano Lett.* **2021**, *22*, 3569–3575.

(27) Luwang, M. N.; Ningthoujam, R. S.; Srivastava, S. K.; Vatsa, R. K. Preparation of White Light Emitting YVO_4:Ln^{3+} and Silica-Coated YVO_4:Ln^{3+} (Ln^{3+} = Eu^{3+}, Dy^{3+}, Tm^{3+}) Nanoparticles by CTAB/n-Butanol/Hexane/Water Microemulsion Route: Energy Transfer and Site Symmetry Studies. *J. Mater. Chem.* **2011**, *21*, 5326–5337.

(28) Grzyb, T.; Szczeszak, A.; Shyichuk, A.; Moura Jr, R. T.; Neto, A. N. C.; Andrzejewska, N.; Malta, O. L.; Lis, S. Comparative Studies of Structure, Spectroscopic Properties and Intensity Parameters of Tetragonal Rare Earth Vanadate Nanophosphors Doped with Eu(III). *J. Alloys Compd.* **2018**, *741*, 459–472.

(29) Liu, L.; Xiao, H.; An, X.; Zhang, Y.; Qin, R.; Liu, L.; Zhang, D.; Sun, R.; Chen, L. Synthesis and Photoluminescence Properties of Core-Shell Structured $YVO_4:Eu^{3+}@SiO_2$ Nanocomposites. *Chem. Phys. Lett.* **2015**, *619*, 169–173.

(30) Ropp, R. C. *Luminescence and the Solid State*, 2nd ed.; Elsevier: Amsterdam, 2004.

(31) Wang, H.; Odawara, O.; Wada, H. Facile and Chemically Pure Preparation of $YVO_4:Eu^{3+}$ Colloid with Novel Nanostructure via Laser Ablation in Water. *Sci. Rep.* **2016**, *6*, 20507.

(32) Hsu, C.; Powell, R. C. Energy Transfer in Europium Doped Yttrium Vanadate Crystals. *J. Lumin.* **1975**, *10*, 273–293.

(33) Moura, R. T.; Carneiro Neto, A. N.; Longo, R. L.; Malta, O. L. On the Calculation and Interpretation of Covalency in the Intensity Parameters of 4f-4f Transitions in Eu^{3+} Complexes Based on the Chemical Bond Overlap Polarizability. *J. Lumin.* **2016**, *170*, 420–430.

(34) Riwotzki, K.; Haase, M. Wet-Chemical Synthesis of Doped Colloidal Nanoparticles: YVO_4:Ln (Ln = Eu, Sm, Dy). *J. Phys. Chem. B* **1998**, *102*, 10129–10135.

(35) Zheng, L.; Huang, X.; Zhong, J.; Wang, Z.; Cheng, X. Upconversion Luminescence and Temperature Sensing Properties of $NaGd(WO_4)_2:Yb^{3+}/Er^{3+}@SiO_2$ Core-Shell Nanoparticles. *RSC Adv.* **2021**, *11*, 3981–3989.

(36) Pollnau, M.; Gamelin, D.; Lüthi, S.; Güdel, H.; Hehlen, M. Power Dependence of Upconversion Luminescence in Lanthanide and Transition-Metal-Ion Systems. *Phys. Rev. B* **2000**, *61*, 3337–3346.

(37) Duée, N.; Ambard, C.; Pereira, F.; Portehault, D.; Viana, B.; Vallé, K.; Autissier, D.; Sanchez, C. New Synthesis Strategies for Luminescent YVO_4:Eu and $EuVO_4$ Nanoparticles with H_2O_2 Selective Sensing Properties. *Chem. Mater.* **2015**, *27*, 5198–5205.

(38) Muto, T.; Takeshita, S.; Isobe, T.; Sawayama, T.; Niikura, S. Photobleaching Properties of YVO_4:Eu^{3+} Nanophosphors Synthesized by Hydrothermal Treatment. *ECS Trans.* **2009**, *16*, 135–140.

(39) Maksimchuk, P. O.; Hubenko, K. O.; Grygorova, G. V.; Seminko, V. V.; Bespalova, I. I.; Soroking, A. V.; Yefimova, S. L. Photobleaching of $LnVO_4$:Eu^{3+} Nanoparticles under UV-Light Irradiation: Effect of Nanoparticle Size. *J. Lumin.* **2022**, *242*, 118593.

(40) Abdesselem, M.; Schoeffel, M.; Maurin, I.; Ramodiharilafy, R.; Autret, G.; Clément, O.; Tharaux, P.-L.; Boilot, J.-P.; Gacoin, T.; Bouzigues, C.; Alexandrou, A. Multifunctional Rare-Earth Vanadate Nanoparticles: Luminescent Labels, Oxidant Sensors, and MRI Contrast Agents. *ACS Nano* **2014**, *8*, 11126 – 11137.

(41) Bouzigues, C. I.; Nguyên, T.-L.; Ramodiharilafy, R.; Claeson, A.; Tharaux, P.-L.; Alexandrou A. Regulation of the ROS Response Dynamics and Organization to PDGF Motile Stimuli Revealed by Single Nanoparticle Imaging. *Chem. Biol.* **2014**, *21*, 647 – 656.

For Table of Contents Only

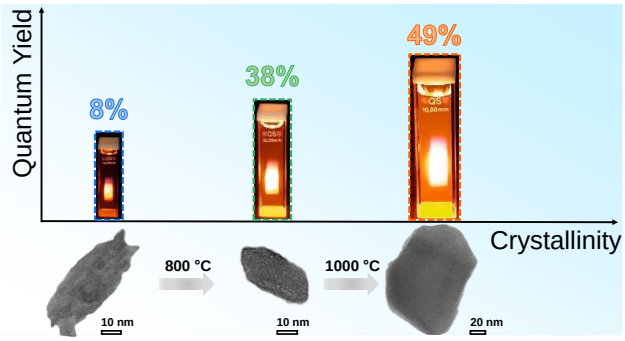

Simple heat treatment of rare earth vanadate nanoparticles promotes crystalline enhancement through intraparticle reconstruction, enabling high-performance luminescent systems